California Central Valley Summer Heat Waves Form Two Ways

Yun-Young Lee[1] and Richard Grotjahn[1]

[1] *Department of Land, Air and Water Resources, University of California, USA*

April 2015, Revised November 2015

Submission to Journal of Climate

---

* *Corresponding author address*:

Atmospheric Science Program, One Shields Ave., Dept. of L.A.W.R. University of California Davis, Davis CA USA 95616Corresponding author email: dolkong400@gmail.com

Keywords: heat waves origin, California heat waves, clustering analysis, wave activity flux

Abstract

California Central Valley (CCV) heat waves are grouped into two types based on the temporal and spatial evolution of the large scale meteorological patterns (LSMPs) prior to onset. K-means clustering of key features in the anomalous temperature and zonal wind identifies the two groups. Composite analyses show different evolution prior to developing a similar ridge-trough-ridge pattern spanning the North Pacific at the onset of CCV hot spells. Backwards trajectories show adiabatic heating of air enhanced by anomalous sinking plus horizontal advection as the main mechanisms to create hot lower tropospheric air just off the northern California coast, though the paths differ between clusters.

The first cluster develops the ridge at the west coast on the day before onset, consistent with wave activity flux traveling across the North Pacific. Air parcels that arrive at the maximum temperature anomaly (just off the north California coast) tend to travel a long distance across the Pacific from the west. The second cluster has the ridge in place for several days prior to extreme CCV heat, but this ridge is located further north, with heat anomaly over Northwest (NW) America. This ridge expands south as air parcels at mid-troposphere levels descend from the northwest while lower level parcels over land tend to bring hot air from directions ranging between the hot area northeast to the desert areas southeast. These two types reveal unexpected dynamical complexity, hint at different remote associations, and expand the assessment needed of climate models simulations of these heat waves.

1. Introduction

Temperature extremes have large impacts on the economy and human safety. A statistically significant increasing trend of about 5% per year in the frequency of billion-dollar disasters is reported in annual aggregates of weather/climate disasters (Smith and Katz 2013). Among them, the adjusted damages related with heat waves/drought total ~210 $B for the 1980-2011 period. Heat waves also cause a large annual number of fatalities (123) on average for the period of 2004-2013 in the US (http://www.nws.noaa.gov/om/hazstats.shtml). There are considerable impacts of heat on morbidity as well. For instance, in Kansas City hospital admissions were increased by 5% during the 1980 heat wave event (Jones et al. 1982).

The California Central Valley (CCV) produces half of the nation's tree fruit and nut crops by both weight and gate receipts. Fruit quality and production can be degraded by hot spells, which causes economic losses to farmers. In addition, the southern CCV has extensive dairy production and extreme heat reduces milk production and cow fertility while raising cow morbidity and mortality. For example, the CCV dairy industry had ~1$B of economic losses from the 2006 heat wave (Bilby et al. 2008). Since the CCV has eight of the nation's top ten most agriculturally productive counties, understanding extreme hot weather over the CCV has great economic and social importance.

Temperature extremes have been linked to some large-scale teleconnection patterns since such large scale wave patterns can redistribute air masses having different temperatures. Particularly during winter, temperature extremes are modulated by the Pacific-North American (PNA) pattern, North Atlantic (or Arctic) Oscillation (NAO or AO), and blocking patterns (Walsh et al. 2001, Wettstein and Mearns 2002, Cellitti et al. 2006, Guirguis et al. 2011, Sillmann et al. 2011). There are substantial modulations of temperature extremes by ocean-oriented climate modes such as the Madden-Julian Oscillation (MJO) (Jeong et al. 2005) and El Nino / Southern Oscillation (ENSO) for the longer time scale (Higgins et al. 2002, Meehl et al. 2007, Alexander et al. 2009, Lim and Schubert 2011). Recent studies clearly demonstrate the geographical dependency of the modulation of temperature extremes by larger-scale teleconnection patterns such as NAO, PNA, ENSO, and the Pacific Decadal Oscillation (PDO) (Loikith and Broccoli 2013, Westby et al. 2013). However, those teleconnection patterns are distinct from the large-scale meteorological patterns (LSMPs) associated with temperature extremes (e.g. hot spells) both in spatial pattern and time scale. As shown in Grotjahn (2011), when the LSMP is present with positive sign and sufficient strength (normalized 'circulation index' >1.6) then CCV extreme surface temperatures usually occur on that day and hence sufficient amplitude of the LSMP is as rare as the temperature extremes. The LSMPs associated with specific temperature extremes are described in far fewer studies (Grotjahn and Faure 2008, Gershunov et al. 2009, Loikith and Broccoli 2012, Bumbaco et al. 2013) than studies of teleconnection patterns. A review of statistical methods, synoptic-dynamics, modeling, and trends relating to temperature extremes in the LSMP context is presented by Grotjahn et al. (2015). The LSMPs for extreme heat events are not fully understood for different parts of North America including the CCV, providing a motivation for this study.

Regional scale heat events may be influenced by land conditions at the surface or below. Land use and land cover change (e.g. from irrigated farm to urban area) can amplify the area experiencing extreme heat (Grossman-Clarke et al. 2010, Wang et al. 2013). Soil moisture deficit strongly contributes to hot extremes in some regions, such as the central United States, Australia and much of Europe (Fischer et al. 2007, Hirschi et al. 2011, Yin et al. 2014). However, soil moisture deficit is not a major factor for the CCV because most farmlands in the CCV are heavily irrigated. The CCV is geographically complex (Fig. 1), where local thermally-driven circulations caused by terrain slope (mountain-valley winds) are mixed with land-sea breezes. Because hot spells are associated with easterly flows (Grotjahn, 2011) air moving in that direction sinks down into the CCV warms adiabatically, and opposes a cooling sea breeze while also lowering the subsidence inversion, and thereby reducing the volume of air heated by surface heat fluxes generated by sunshine.   These conditions all favor the formation of extreme hot spells.

Prior studies found that summertime hot spells in the CCV area are closely linked to LSMPs that are an equivalent barotropic, nearly-stationary wave train (ridge-trough-ridge) across the N. Pacific and western N. America (Grotjahn and Faure 2008, Grotjahn 2011, 2013). Grotjahn and Faure (2008) describe the formation of the hot spells LSMP with apparent westward wave motion (on the southern part) and eastward development from a west Pacific ridge to a mid-Pacific trough then a North American west coast ridge (on the northern part) using composite maps prior to onset of 18 extreme events over 22 summer seasons. Grotjahn (2011) defined a metric to identify how similar a given day's weather pattern matches the hot spells composite LSMP from 1979-2010. This study extends the period of study of CCV hot spells LSMPs and examines them more closely.

A primary question considered in the current study is: what is the source of the hot air present in the heat wave? This question led the authors to calculate backwards in time trajectories. It was immediately apparent that the trajectories of CCV hot spells are roughly divided into two groups. The next question is: do those two paths represent two distinct ways to generate CCV hot spell conditions? Using objective tools, this paper classifies CCV hot spells into two types based on the temporal and spatial evolution of LSMPs, provides direct statistical and structural comparisons between the two types, and uncovers some key dynamical differences that lead to the distinct types.

The paper organization is as follows. Section 2 outlines the dataset and methods used. Section 3 presents the classification of two different types of CCV heat waves and corresponding LSMPs. Section 4 provides the dynamical differences that drive two distinct hot spells. Lastly, section 5 summarizes the results.

2. Data and Methods

2.1 Synoptic and Reanalysis dataset

This study uses daily maximum near surface temperature from 15 NCDC stations (in Fig. 1). Among 23 stations, five stations are excluded due to their location in the ‘Delta’ a region where weak sea breezes can provide local, short interruptions of heat waves that are not experienced elsewhere in the CCV. Three more stations are excluded for being close to other NCDC stations thereby creating a relatively even distribution of stations over the CCV (these 8 stations are omitted in Fig. 1).

This study analyzes upper-air LSMPs derived from the National Centers for Environmental Prediction – National Center for Atmospheric Research reanalysis 1 dataset (NNRA1) (Kalnay et al. 1996). Time and spatial resolution of NNRA1 is 6 hourly and 2.5 degrees longitude by 2.5 degrees latitude. We consider boreal summer season extending from June through September (JJAS, 122 days) and the time period from 1977 to 2010 (34 years). The choice of data and time period was a compromise between having more events (larger sample) while also maintaining relatively high accuracy of the reanalysis data due to the assimilation of satellite observations.

2.2 Event isolation

Space and time criteria are used to identify CCV hot spell events from the NCDC station data. By considering duration time and spatial coverage together, this method isolates those events in which a majority of CCV stations experience hot weather commonly for sufficient time. The method is as follows: 1) calculate 15 stations' daily maximum temperature anomalies (relative to each station's long term daily mean), 2) normalize these anomalies by long term daily mean standard deviation for each station, 3) select the 5% hottest dates for each station, 5) retain those dates common to at least six stations, 6) isolate events when there are both at least three consecutive retained dates in a row within JJAS and the interval between two events is six days or longer. The six-day interval was chosen based upon the autocorrelation function being <0.05 for all CCV stations collectively and nearly all individually for lead or lag times greater than six days (see Fig. S2 in the supplementary material). This process identified 28 heat wave events for the CCV (Table 1). Dividing the 1977-2010 data into four periods: three 9-year periods followed by a 7-year period, finds an approximately even distribution of hot spell occurrences, 7, 8, 6, and 7 respectively. This space and time method detects heat waves based on extreme temperatures across the CCV but it results in a small sample size of about one event per year. The intention behind choosing such rare events is that the dynamics responsible for these extremes will have a stronger signal amongst the 'noise' of natural variability.

Consistent with Grotjahn (2011) we assign the onset for every event to be 12 UTC. Although 0 UTC (the next day) is closer to the local time (23 UTC) of highest surface temperature, upper air charts at the earlier time (12 UTC) have more predictability (Grotjahn, 2011).

2.3 Identification of distinct LSMPs prior to heat wave onset

2.3.1 Backward trajectories

Prior work (Grotjahn and Faure, 2008, Grotjahn, 2011, 2013) found the maximum upper air temperature anomaly (at 850 hPa) to be centered just off the west coast of North America, near the California/Oregon border. Backwards trajectories from this area of highest temperature (plus analysis of individual terms in the temperature equation, not shown) were calculated to answer the question of how do the high temperatures develop there. The backward trajectory calculation uses six-hourly reanalysis data. The procedure starts with identifying 3-dimensional wind (u_1, v_1, ω_1) and elevation estimation (z_1) hypothesizing hydrostatic balance in a homogeneous atmosphere at six grid points (the combinations of two longitudes (122.5W and 125W) and three latitudes (35N, 37.5N and 40N) at 850 hPa at the onset time. The three-dimensional wind field is used to estimate the distance travelled over the prior six hours. The scheme includes the convergence of meridians when calculating zonal distance travelled. The scheme finds a first guess $(\theta_2, \varphi_2, p_2)$ of each parcel location six hours before by subtracting the longitudinal, latitudinal and pressure distances from the original location $(\theta_1, \varphi_1, p_1)$. Next, the three-dimensional wind (u_2, v_2, ω_2) is estimated at the first guess location by applying bilinear interpolation. The final location $(\theta_0, \varphi_0, p_0)$ of each air parcel six hours before the original time is estimated by calculating again the longitudinal, latitudinal and pressure distances from the averaged 3-dimensional wind $(\frac{u_1+u_2}{2}, \frac{v_1+v_2}{2}, \frac{\omega_1+\omega_2}{2})$. Those procedures are repeated for prior times in steps of six hours totaling several days. The locations are plotted as projections onto two-dimensional planes in a trajectories diagram. The trajectories diagram (shown later) plot one average patch calculated from these six paths for each event. The individual and the average trajectories appeared to identify two different types of paths that lead up to a similar LSMP at the event onset. Grouping the cases based on these two types of paths, and after close inspection of the fields of individual events, we chose portions of three anomalous fields as 'target fields' for the hot spell classification: 700 hPa zonal wind at two days lead, 600 hPa temperature at two days lead, 700 hPa temperature at one day lead over 150W-100W, 20N-60N domain.

2.3.2 Clustering techniques

Clustering analysis is able to group similar patterns prior to onset among 28 events, therefore providing a quantitative tool to isolate distinct origins of the heat waves. In this study, the k-means clustering technique is applied to the 'target fields' defined above. Simply, this is an iterative algorithm moving events from one group to another until there is no additional improvement in minimizing the overall distance between patterns among events in resultant groups. The 'distance', for instance, can be defined as the squared Euclidean point-to-centroid distance in a group, where each centroid is the mean of the patterns in its cluster (Spath 1985, Seber 2009). This method has been widely used in the atmospheric research not only associated with the relationship between LSMPs and extreme weather (Park et al. 2011, Stefanon et al. 2012) but also for assessing the climate model performance (Lee and Black 2013, Westby et al. 2013). It should be noted that cluster results can be strongly dependent on the selection of the target fields to be used by the cluster analysis. (However, in a companion study submitted elsewhere, using other levels retrieved the same cluster memberships.) In every iteration step, the clustering procedure creates clusters objectively, but the process is not entirely objective as the target fields are chosen a priori and those choices make the calculation partly self-referential.

Two concerns arise when applying k-means clustering to atmospheric extremes because: a) there is uncertainty in choosing an optimal number, k, of clusters and b) assigning an event to one cluster rather than another is less clear when the sample size is small. To address these concerns we used the distinctly different backwards trajectories to make an initial partitioning of cases. Next we examined the composites and very different evolutions of the LSMPs were clearly apparent. Then we decided to apply spatio-temporal cluster detection to a small number of variable and level combinations at times shortly before heat wave onset. We applied an analogy of ‘distance of dissimilarity’ metric (as in Stefanon et al. 2012) to judge the optimal number of k. The number k with an abrupt drop of inter-cluster distance for the next higher value (k+1) is considered the optimal number of clusters. Inter-cluster distance of our target fields has a notably abrupt drop from k=2 to higher k (not shown). A larger number for k may represent less ambiguity in the classification. However, clustering analysis aims mainly to gain a physical insight for heat wave formation which is possible with a minimal number of distinct groups and not a separate group for every single event. The distance of dissimilarity metric as well as our qualitative analyses of trajectories led us to choose k=2 clusters in this study. In addition, spatial projection analysis is applied to assess how well individual events sort into the two clusters. Projection coefficients ($p_{k,j}$) of the j th event against the k th cluster composite means are calculated for the same domain of the ‘target fields’ above.

$$p_{k,j} = \frac{\sum_{i=1}^{N}\left(x_i^j y_i^k\right)}{\sum_{i=1}^{N}\left(y_i^k\right)^2}, \;\; for\; k = 1{,}2 \;\; and\; j = n$$

where k is a cluster, j is an event, i is a grid point, n is the total number of event, N is the total number of grid points and x is the field of a variable of individual events (j) to be projected and y is the composite mean field of x for two clusters. The projections are plotted as a scatter plot such as Fig. 2. In the scatter plot, one sees that individual events do seem to fall into groups where the projection on one cluster mean is much higher than the projection onto the other cluster mean. However, some events have LSMP structure that does not strongly favor one cluster mean over the other. These ‘mixed’ events were identified as follows. Initially, the maps for all events were processed with a clustering algorithm detailed above using k=2. Then cluster averages were formed from the members of these two clusters. Using those cluster means, each event was projected onto both cluster means. The membership of each cluster was revised by requiring the new projection of an event onto that cluster be more than twice the projection of that event onto the other cluster mean. Events that did not satisfy the 'twice projection' criterion were identified as 'mixed' events that tend to be a mixture of both types of clusters. Such 'mixed' events were then excluded from the final cluster definitions, thereby isolating more strongly the two types of clusters. Of the 28 events during this time period, 5 'mixed' events were so excluded. After excluding the mixed events, new cluster composites were calculated from the two revised clusters of events and projection coefficients were calculated again with respect to these new cluster composites and plotted.

2.3.3 Wave activity flux

This study analyzes the wave activity flux (WAF) as defined by Takaya and Nakamura (2001) to track the propagation of wave energy. Unlike the E-P flux (Edmon et al. 1980) and the wave activity flux developed by Plumb (1986), this method allows one to make a "snapshot" analysis as it does not include any time averaging. Therefore, the time evolution is tracked of the wave activity associated with development of each heat wave. Under a conservation law, the wave activity is related with the wave enstrophy and wave kinetic and internal energy and part of those two factors is closely connected to the temperature. Since this method assumes a linear geostrophic stream function ($\psi=\Phi/f$), the wave activity is also related to the geopotential (Φ) perturbation. Takaya and Nakamura show that this WAF is locally parallel to the group velocity of quasi-geostrophic Rossby wave packets. The WAF vectors show movement of co-located geopotential ridges and troughs. One might approximately interpret daily weather charts as follows: convergence of WAF at a ridge in geopotential height is expected to amplify the ridge to the extent that the ridge is a deviation from a horizontal mean field. (Local change of wave activity is proportional to convergence of WAF if one neglects diabatic effects.) The same geopotential ridge would decay if WAF was diverging there. Depending upon where the WAF convergence and divergence occur relative to the geopotential pattern, the WAF convergence and divergence zones can be interpreted as driving propagation as well as amplitude changes of the troughs and ridges. The Takaya and Nakamura WAF formulation has been applied to understand the dynamics of many phenomena. For example, the converging of wave activity flux into the amplifying blocking ridge and attendant wave activity flux divergence upstream of the blocking ridge is known to influence the blocking formation over Siberia (Nakamura et al. 1997, Takaya and Nakamura 2001). Here, the WAF is used to interpret the temperature increase and corresponding ridge formation along the North American west coast that is associated with hot spells.

2.3.4 lead-lag composite

Another tool used to understand the time evolution is to form composites of total and daily anomaly fields of atmospheric variables and WAF for individual clusters at fixed times prior to the event onset time. These clearly show differences between the clusters in temporal and spatial development of corresponding LSMPs and related dynamics. Although the sample size is small for each cluster, the patterns and their evolution are consistent among the events within a cluster. The consistency is measured by counting the number of events with same sign of the anomaly at each grid point, a procedure called ‘sign-counts’ (Grotjahn 2011). Sign counts are calculated as follows: in a cluster, the number of events with negative sign at a grid point is subtracted from the number of events having positive sign at that grid point, that difference is then divided by the total number of events in that cluster to facilitate comparison among clusters having differing numbers of events. Hence, a sign count of 1.0 means all events in that cluster have positive anomaly at that grid point. A sign count of -1/3 means two thirds of the events have negative anomaly at that grid point.

3. Two Different Types of CCV Heat Waves

3.1 Classification of CCV heat wave events

The heat waves selection criteria identify 28 events in the period 1977-2010. These events can be grouped into two types by K-means clustering techniques discussed in section 2. The first cluster has 13 members while the second cluster has 10 events. Both clusters are spread relatively evenly over the 34 summer seasons studied although the first cluster (identified with asterisks in Table 1) is more common in the decade of 2001-2010. Regarding the duration days of events, the second cluster shows shorter persistence (3.8 days) on average than does the first cluster (4.2 days) although this duration difference is not significant at 95% confidence level. To ensure the fidelity of the two groups, apart from the 'dissimilarity index', spatial projection coefficients of individual LSMPs are calculated for each of the two revised cluster composites and their distribution plotted as a scatter diagram in Fig. 2. Since the spatial projection coefficient indicates similarity of the shape and magnitude, the fidelity of dividing events into groups is apparent by (a) individual events have at least more than twice as large coefficient in one cluster composite than the other, (b) events tend to collect in groups, and (c) the groups are distinctly separate on the scatter plot. The two types of heat waves grouping satisfy these three conditions very well. However, of the 28 events, five events are mixtures of the two types are excluded from the analyses after this point.

3.2 Temporal and spatial evolution of anomalous LSMPs: temperature, horizontal wind, and omega

This study focuses on LSMPs during the two different ways CCV heat waves develop, therefore the focus is upon anomalous fields of air temperature, horizontal wind and omega (equivalently the 'pressure velocity', meaning vertical motion in isobaric coordinates) at three pressure levels (850, 700, and 600 hPa) for several days prior to the event onset. These time and space domains are consistent with those used by the clustering analysis. At onset time, both clusters (contours in right hand column in both Fig. 3 and Fig. 4) commonly have a peak of temperature anomalies (TA) centered near but off the Northern California coast and extending outward, including over the CCV area (this region is hereafter called the "TA area"). The domain enclosed with long-dash in Fig. 1 s TA area. Grotjahn (2011) emphasizes the consequences of a warm temperature anomaly in the TA area as it creates a thermal low at the coast and the low level pressure gradient opposes a sea breeze from cooling the CCV. While there is similarity in the TA area at onset, elsewhere the differences between clusters in the spatial coverage and magnitude of the temperature anomalies are remarkable. In the first cluster strong warm anomalies cover mostly California with a lobe into the eastern Pacific (Fig. 3). In the second cluster the strong warm anomaly has a lobe over northwestern America including a second peak over Washington State (Fig. 4). In magnitude, this ensemble mean temperature anomaly at 850hPa is hotter in the second cluster than in the first cluster. At higher levels the temperature anomaly is a bit weaker over the TA area in the second cluster though the peak values are higher in cluster two and an anomaly is centered some distance to the northeast of the area.

Leading up to the event onset, one main difference between the clusters is cluster two has a hot spell over NW America before the CCV hot spell onset. The second cluster has very strong equivalent barotropic warm anomaly through the depth of the troposphere for several days prior to the onset. The first cluster does not have this pre-existing hot anomaly, but develops it first over the TA area. In the second cluster, a part of that Northwestern US hot spell's southern tail expands over the CCV area; as the NW hot spell weakens the TA area temperature anomaly amplifies especially in the lower troposphere.

Anomaly omega composites show a significant zonal dipole of rising-sinking motion in both clusters (shadings in Fig. 3 and Fig. 4). The second cluster has stronger dipole that is centered at a higher latitude at two days lead than the dipole in the first cluster which peaks at one day lead. Sinking motion located over the land mass is very important to the formation of the temperature maximum in the TA area due to adiabatic compressional heating. The first cluster shows local subsidence of air at the north boundary of the TA area that increases over time until just before onset. The second cluster has very strong sinking motion covering much of inland western North America during 2.5 to 1.5 days lead; at onset the sinking wanes to the north and waxes over the north and east half of the TA area. As detailed in Grotjahn (2011), this local sinking motion is crucial for the intensification of the CCV hot spells due to adiabatic compression and by lowering the climatological summertime subsidence inversion.

Formation of the heat wave in both clusters is linked to horizontal advection of the anomalously hot air. The anomalous horizontal flow upstream of the TA area is generally coming from a region of anomalous sinking motion (Figs. 3 and 4). However, the direction of that motion is distinctly different between the two clusters (vectors in Figs. 3-6). Total fields (Figs 5-6) clearly show the diurnal cycle in both clusters. The time 0 UTC (2.5, 1.5, and 0.5 lead days) is close to the local time of highest surface temperature. Along with the diurnal cycle, one might expect a sea/land breeze. At the onset and 850hPa level, the total fields show offshore or along shore flow in the total fields (Figs 5-6) with anomalous easterlies in the TA area (Figs. 3-4)

For the first cluster, at later stages (1.5 days lead to onset), winds approach the TA area from a southwesterly direction. The wind direction then turns northwesterly or northerly while passing through an area of strong subsidence on the northwest side of the TA area (Fig 5) incorporating the enhanced subsidence to the north (Fig. 3). In Fig. 3 the sinking anomaly is strongest in the afternoon (-1.5 and -0.5 days) counteracting diurnal rising that otherwise might occur. Prior to that time (2.5 and 2.0 days lead), there is anomalously strong southwesterly flow offshore (Fig 3) that amplifies a strongly westerly total wind (Fig. 5). Backwards trajectories (Fig. 7) will link these motions leading to paths that are crossing the eastern north Pacific before turning southward and sinking near the TA area.

In the second cluster the anomalous flow several days prior to onset (2.5-1.5 days lead) is strongly southerly becoming southeasterly at the west coast (Fig. 4) such that the total flow near the coast (Fig. 6) is much weaker (and many places has opposite direction) at the TA area than in the other cluster. As with the other cluster, the motion that reaches the TA area passes through sinking off the west coast (Fig. 6) though prior to onset most of the sinking is centered on the south side of the TA area. Anomalous sinking (Fig 4) opposes rising (Fig. 6) over the Rockies for several days prior to onset; only at onset does the anomalous sinking (Fig. 4) enhance subsidence at the TA area (Fig 6). The weak total winds means that air parcels in the TA area do not travel far. The anomalous winds are southeasterly in southern Nevada and southern deserts of California and also have an easterly component in northern: Nevada and California (Fig. 4). The centering of the sinking on the southwest side of the TA region (with southerly and southeasterly winds) followed by sinking on the north side (with northerly winds) at onset suggests cluster mean parcels will come from the south and east in cluster two. Backwards trajectories (Fig. 7) show the properties just anticipated: these trajectories generally do not sink as much as those in the other cluster, their horizontal distances traveled are less, and the direction traveled has more variation between events in this cluster. However, several of the trajectory paths of cluster two arrive at the TA area from the desert region to the southeast. Cluster two has strong westerlies, similar to cluster one, but they are located much further north due to the pre-existing temperature anomaly (and geopotential ridge) centered near northwestern North America.

Air parcels that arrive at 850 hPa in the TA area are tracked over 4 days prior to onset by the backwards trajectory scheme described in section 2. The average path for each event is plotted in Fig. 7. The paths are consistent with motions anticipated in the discussion of the LSMP wind components above. Most air parcels in cluster one move from the west while sinking as they approach the TA area before heat wave onset. Two paths have brief periods of rising motion before sinking (events 7 and 22). Other paths approach the TA area from the south, east, or northeast (events 3, 9-11, 15, 17, and 27); these paths are all in cluster two. Different starting heights were tested for each event. Fig. 7 uses 850hPa for the starting level and the paths descend to that level from pressure levels commonly between 600 hPa and 800 hPa with 500 hPa being the maximum height. Trajectories in the second cluster have lower maximum heights than trajectories in the first cluster on average. Specifically, half of the events (5 out of 10) in cluster two have paths traced backward that stay below 700 hPa, while most events (10 out of 13) in cluster one have paths descending from elevations above 700 hPa. However, one of those 3 Cluster one paths traced back to 700-800 hPa had peak elevation of 600 hPa before descending to the starting location at 850hPa. Also as anticipated, the two clusters show very different paths and origins zonally before onset. Paths in the first cluster (dashed paths) four days prior to onset often start west of 140°W (with three exceptions). In contrast, paths in the second cluster (solid paths) travel a short zonal distance and all trajectories remain east of 140°W. Five paths in the second cluster start east of their final location. In the meridional plane, a half dozen paths in the second cluster reach the TA area from the region encompassing the Great Basin, Mojave, and Sonoran Deserts, while other paths arrive from the west, northeast, or hardly move. In the first cluster the starting latitudes of paths are rather evenly spread. There appears to be a tendency for parcels in the first cluster to sink from a higher elevation when traveling from a higher latitude to reach the TA area.

Some differences in the total fields LSMPs of the two clusters (Figs. 5-6) are worth emphasizing. In the first cluster: upstream of the west coast, strong west-southwesterly flow extends across the domain at higher latitudes. Further south, the upper level winds weaken and become more northwesterly as the temperature anomaly develops near the west coast. Development of the temperature anomaly in the TA region by onset time appears due to this long-lasting northwesterly flow that also continues to pass through a northwest-southeast oriented region of strong sinking off the west coast and paralleling the coast. In contrast, the flow in the second cluster is weaker all along the US west coast and has a southerly component at the west coast (at 700 and 600hPa) with evidence below (850hPa) of southerly or even southeasterly motion over land but northerlies offshore on the east side of the subtropical high. All paths are again passing through areas of sinking (though the anomalous sinking is generally far from the TA area except at onset) just upstream from where the temperature anomaly is growing; in cluster two that is on the southwest side of the pre-existing NW America anomaly. In the second cluster the total field shows a correspondence between the vectors on the southwest corner of the NW America temperature anomaly that cross the broad area of enhanced sinking as the thermal anomaly expands on its southern side. In both clusters, the broad areas of sinking that paths traverse are more apparent in the daytime maps. Rising motions over the Rockies to the California Sierra Nevada mountains during the afternoon are reduced by the anomalous sinking in both cases though the timing relative to onset varies. At 600 and 700 hPa, high latitude strong westerlies persist in both clusters. In the second cluster, the westerlies are shifted poleward owing to the pre-existing NW America thermal anomaly. The flow in the southeastern part of the domain also differs, having a stronger southeasterly flow component in cluster two, consistent with some of the trajectories reaching the TA area coming from the southwest deserts.

These motions and temperature differences leading up to onset are consistent within each cluster and distinct between clusters. Fig. 8 shows box and whisker plots using NNRA1 and ERA-interim reanalyses over select regions and times. In Fig. 8a, the cold anomaly to the north in cluster one versus the warm pre-existing hot anomaly in cluster two are obviously distinct at 700 hPa one day prior to onset. In Fig. 8b, 1.5 days before onset, the weak westerlies over the TA area are evident in cluster one, while cluster two events have net easterlies in the same region at 700 hPa. In Fig. 8c, two days prior to onset at mid-tropospheric levels to the NW and partly encompassing the TA area, weak southerlies occur in cluster one but strong northerlies occur in cluster two. In all cases the two reanalyses have very similar distributions. For 850 hPa temperature anomalies, a corresponding plot (not shown) over the TA region at onset finds complete overlap of values among the events and between both clusters for both reanalyses since events detection is basically based on near-surface standardized temperature anomalies

4. Dynamical Differences Driving Two Types of Heat Waves: WAF and Jet Stream

The discussion above connects temperature anomalies, air motions, sinking and strong adiabatic compressional warming. A key difference between the two types is that greater sinking over the TA region is required in Cluster one since the air parcels are of maritime origin; in Cluster two the parcels arrive from a region of pre-existing warm air in the interior West. A more dynamical picture is presented here that reinforces the discussion above. In addition, the domain is expanded to provide a larger context for the heat waves development in these two clusters.

Since all events have high heat over the CCV, the strengths of West Coast ridge in the two clusters are similar at onset time. It is the differing evolutions prior to onset time that are of interest. Prior to onset, the two clusters have different wave patterns spanning the North Pacific in the composites of 500 hPa geopotential height anomalies (Fig. 9). The primary difference is the existence of a persistent, strong, West Coast ridge in the second cluster versus development of that ridge in the first cluster. For the first cluster, an initially very weak ridge located west of California over the subtropical ocean strengthens and expands northward. Simultaneously, a north Pacific trough reduces its eastern extent, which implies the wave energy propagation towards the west coast. For the second cluster, positive height anomalies peak over NW America at 2-1.5 days lead. After that, the highest values in the ridge weaken, the area expands southward, and its center moves southwestward, concurrently the North Pacific trough decreases in strength until lead day 1.5 then increases again while drifting westward. From 2 days lead to onset, the zonal wavelength of the wave train is shorter in the first cluster than in the second cluster. The wave pattern is more zonally-oriented in the second cluster whereas the pattern follows more of a great circle route in the first cluster. Further upstream, the LSMP in cluster number two shows a significant trough in the subtropics near the east coast of Asia (2.5-1.5 days lead). The trough near Asia may imply a connection to the tropics that is not further explored in this paper. As this near-Asia trough diminishes, the western North Pacific ridge strengthens and moves eastward while (as mentioned) the central North Pacific trough weakens and retreats slightly west. From 1 day lead, the central North Pacific trough becomes strong again while the two neighboring ridges become weak. These results imply that the energy propagation is not simple and more complicated in the second cluster.

Fig. 9 also shows cluster-mean WAF vectors for times prior to and including event onset. The WAFs differ between the clusters in ways consistent with the discussion above. In the first cluster, there are southeastward WAFs from the southern side of the mid-ocean trough that become progressively stronger as onset is approached. The WAFs cross Pacific with clear convergence in the eastern Pacific that is consistent with the building of the West Coast ridge. In the second cluster, WAF vectors are somewhat stronger through most of the period. Close to onset time WAFs on the south side of the mid-ocean trough amplify the southern side of pre-existing west coast ridge. Far upstream, the WAF off the Asian coast from the trough there builds the west Pacific ridge that is stronger and further south in cluster two prior to onset. In cluster one, the south side of the west Pacific high grows later, closer to onset.

Given the different anomaly patterns in mid-tropospheric geopotential, one expects differences in the Pacific jet stream, as well. Fig. 10 shows total zonal wind and zonal wind anomaly at 250 hPa, separately analyzed for the two clusters (shading for anomalies and darker contours for total fields). Anomaly winds at 250 hPa, the 500 hPa geopotential heights (Fig 9), and the lower level total horizontal winds (Figs. 5-6) all have anti-cyclonic flow over the North American west coast and further upstream all have a mid-ocean trough, hence the LSMPs have equivalent barotropic structure as noted before (e.g. Grotjahn and Faure, 2008). The equivalent barotropic structure of the wave train in each cluster is also confirmed from height anomaly patterns plotted at all significant levels in the troposphere (not shown).

In the first cluster, the northern dipole pair of wind anomalies in the eastern North Pacific expand and push the Pacific Jet southward in the mid Pacific and northward in the eastern North Pacific before event onset. The downstream expansion amplifies the total zonal component whose value peaks at lead day three. Subsequently, the jet stream peak value diminishes while moving eastward, producing a clear deceleration region located offshore at latitudes 35-50N that also moves eastward. From a simple momentum equation argument, this jet stream deceleration (jet streak exit) region could have southward ageostrophic motion. Ageostrophic northerlies at the jet exit coupled with little ageostrophic wind to the south that migrates eastward across the northern US seems consistent with a similar migration of sinking seen in Fig. 5. Further south, the easterly wind anomaly migrates northeastward towards the TA area as the thermal anomaly builds. In the second cluster westerly anomaly winds build the jet stream much further north (western Canada) and easterly anomaly winds suppress it near the west coast of America (where the large temperature anomaly resides for days prior to onset). That thermal ridge over the west coast in both cases has easterly wind anomaly over Southern and Baja California, that anomaly creates a small zonal variation of the zonal wind there. In a simple zonal momentum equation argument, a deceleration of easterly flow requires a southerly ageostrophic flow. Therefore southerly ageostrophic winds could prevail in this region. Ageostrophic northerlies in the deceleration region of the Pacific Jet coupled with ageostrophic southerlies where the North American Jet accelerates (further south) create upper level convergence and sinking beneath as deduced from simple vorticity arguments (e.g. Grotjahn and Osman, 2007) and as seen in Figs. 3 and 5 for the first cluster. That more southern jet location in the eastern Pacific seems consistent with the longer trajectories in the first cluster (though the jet is at a higher level than those paths). In the same manner, trajectories travel shorter distances in the second cluster which seems consistent with downstream weakening of the zonal winds along the US west coast.

On the opposite side of the Pacific, the westerly jet stream (Fig. 10) near the Asian coast curves much further north in cluster two, reflecting the stronger ridge (Fig. 9) in that region. In cluster one the jet stream is contiguous from the east Asian coast across the Pacific and into North America. In contrast, the connection to the east Asian jet becomes severed as onset approaches in cluster two. A larger amplitude wave train is present at this elevation for cluster two, as well.

The LSMPs have a large scale wave train and we have been asked if these LSMPs are similar to well-known ‘teleconnection patterns’. However, teleconnection patterns are based on longer term variations in the circulation rather than the shorter term fluctuations with extreme, highly episodic events. Moreover, most teleconnection patterns identified and cataloged by climatologists are based on analyses of the fluctuations in the wintertime flow. Nevertheless, we tested similarities to eight summer season teleconnection patterns (see http://www.cpc.ncep.noaa.gov/data/teledoc/telecontents.shtml) by calculating pattern projection coefficients for 10 days leading up to the event onset over the region 20°N-60°N, 120°E-90°W where the LSMP wave train has large amplitude. It should be noticed that several of these teleconnection patterns have their larger amplitude outside the domain used in this calculation, so this test artificially magnifies the pattern projection for those teleconnection patterns.

For the North Atlantic Oscillation (NAO) and Scandinavia patterns, averages of all events and each cluster mean and individual events show almost zero projection at the times tested (see Fig. S1 in the supplementary material). For the West Pacific, East Pacific-North Pacific,

Pacific/North American (PNA), and East Atlantic/Western Russia patterns, projections vary slightly with time and between the two clusters. However, they are not significant since the values of the means are much smaller than the variation among events. For the East Atlantic pattern, three averaged projections of all events and two cluster members increase as time approaches the heat wave onset although the variation among events is much larger; even so, the projections have small values (<0.15 in all instances). Positive projection at the onset day might be considered significant since a majority of events have the same (positive) sign of projection coefficients. The reason for the (weak) positive projection is that the East Atlantic loading pattern has a strong west coast ridge over North America like the heat wave LSMPs do. For the Polar/Eurasia pattern, negative projection from 4 days prior to onset is common among the events. The loading pattern of Polar/Eurasia has a zonal dipole over the high latitude North Pacific and this pattern is almost opposite to the pattern of heat wave LSMPs as shown in Figure 9. Therefore, most events show negative projections. However, the main domains of the East Atlantic and Polar/Eurasia patterns are where the heat waves LSMPs are weak and those domains are outside the Pacific sector used in this calculation. So the LSMPs' similarities in this sector seem to be little-related to East Atlantic and Polar/Eurasia patterns. In summary, this projection analysis shows little relation between these heat wave LSMPs and most of the teleconnection patterns. However, this result does not preclude a teleconnection pattern from reinforcing the heat wave associated with the LSMPs.

5. Summary and Further Discussion

This study examines recent summer heat waves of the California Central Valley. This study focuses on three main issues: 1) spatial-temporal detection criteria of heat waves using normalized daily maximum surface temperatures of 15 CCV NCDC stations, 2) validity of grouping CCV heat waves into two clusters based on noting differences in the LSMPs' evolution, and 3) examination of the LSMPs' properties with emphasis on the distinctly different formation of each cluster of heat waves.

Using normalized daily maximum surface temperature anomalies at 15 NCDC stations, 28 heat wave events were identified when at least 6 stations surpass the 95% level for at least 3 days. After examination of three-dimensional backwards trajectories and weather maps for each individual event, k-means clustering was applied to the merged anomalous field consisting of 700 hPa zonal wind (2 days lead), 600 hPa temperature (2 days lead), and 700 hPa temperature (1 day lead) over the domain: 150W-100W, 20N-60N. After testing several numbers (k) of clusters, two groups (k=2) proved to be reasonable from the calculation of the inter-cluster distance metric. A projection analysis was also applied to check the reliability of k-means clustering results. A scatter plot of projection coefficients of individual events onto each of the two cluster composite fields finds two groups that are well separated with sufficient distance and events in a group to justify the clustering and to perform useful analyses. Among the 28 events during the 1977-2010 period, five events are 'mixed events' not clearly associated with just one cluster; these events are excluded in the analysis. The final ensembles have 13 members in cluster one and 10 in cluster two.

Composite analyses are made of air temperature, horizontal wind, and omega for the two clusters at three vertical levels and on 6 lead times including the onset time. These composite analyses focused upon a region centered near the northern California coast, the 'TA area' which has been shown to be crucial for CCV heat waves (Grotjahn, 2011). (A thermal low in sea level pressure there opposes a cooling sea breeze.) One difference between the two clusters of temperature anomalies is the warm anomaly is slightly stronger in the second cluster than in the first cluster. The temperature anomaly has a southwest lobe in the first cluster and long northeast lobe in the second cluster. In the first cluster, warm anomalies in the TA area begin to form in the TA area rapidly strengthening in the final 1.5 days before onset. The second cluster has a pre-existing strong temperature anomaly to the north of the TA region; this anomaly becomes latitudinally elongated as a lobe develops southward, extending over the TA area during the 2.5 days prior to onset time. While the temperature anomaly increases over the TA area, the northern end of the preexisting anomaly migrates eastward creating that lobe in in cluster two. The CCV heat wave follows the heat wave occurring in NW America for events in this second cluster. This link to NW America explains why Bachmann, 2008, found extremely hot days in Sacramento match dates of extremely hot days better in Seattle than in much closer Reno. After the peak of NW heat wave, warm anomalies expand over the TA area by flow that passes through areas of enhanced sinking sometimes from south of the TA region but usually without travelling as far as air parcels in cluster one.

In both clusters, although the pattern varies, the high temperatures result from compressional heating as horizontal winds bringing sinking air to the TA region. Anomaly fields of sinking and horizontal motion help interpret the total fields of motion. The sinking adiabatically warms the lower troposphere and especially over land lowers the subsidence inversion. Solar heating rapidly raises surface station temperatures during the daylight hours because the surface heat flux is mixed into the shallower than usual layer below the subsidence inversion. In cluster one, the sinking anomaly is located to the northwest and to northeast of the TA area where northerly and northeasterly anomaly winds occur. Upstream to the west, the wind anomalies are strongly southwesterly. When added to the long term daily mean winds, these wind anomalies create a total wind that has strong westerlies upstream that turn to become northwesterly as the air encounters unusually strong sinking centered at or off the west coast of the US. These northwesterlies are pointing towards the TA area, building the temperature anomaly rapidly there. Higher up, sinking over the TA area is consistent with ageostrophic wind convergence resulting from the Pacific jet exit region to the north and the North American jet entrance region to the south. In cluster two, the pattern is more complex. There is anomalous sinking to the east of the TA area and small velocities from south and east. Total horizontal flow is quite mixed, as mid tropospheric levels have sinking and southwesterlies on the north side of the TA area, while below (850hPa and below) there are northerlies in this area of sinking. On the south side of the TA area, there are southeasterly and easterly total winds, again passing through an area of sinking during afternoon. The somewhat opposite directions that slow moving, sinking air takes to build the temperature anomaly in the TA area contrasts with the simpler pattern of cluster one and shows up strikingly in air parcel trajectories.

Trajectories moving backwards in time were calculated to trace the origin of air parcels arriving at onset in the TA area at 850 hPa. The two clusters show clear differences in the origins and travelling distance of these air parcels. Air parcels of the first cluster often travel eastward across much of the North Pacific, while air parcels of the second cluster are less consistent but include parcels moving out of the desert to the southeast. The far west origins of most air parcels in the first cluster are consistent with the eastward extension of the Asian jet stream compared to the second cluster. Since the spatial resolution (2.5 degrees in latitude and longitude) of the NNR1 data is somewhat coarse both horizontally and vertically, one may suspect the accuracy of trajectories and the robustness of this separation of trajectories between two clusters. This concern was checked by applying the trajectory calculation to the higher resolution reanalysis of

ERA-Interim2 (Dee et al. 2011). ERA-Interim2 data have 1 degree by 1 degree resolution. Trajectories based on ERA-interim2 data have similar primary properties: members consistently have longer traveling distances (eastward over the Pacific) in the first cluster while in cluster two trajectories again move slowly and come from various directions including originating in the desert to the southeast. Again, the ERA-interim2 paths pass through regions of sinking just prior to reaching low elevations in the TA area (not shown). Hence all the main characteristics of the trajectories for these two clusters are not sensitive to the reanalysis data type and/or model resolution.

Temporal and spatial evolution of height anomalies and wave activity fluxes in the middle troposphere (500 hPa) show the eastward energy propagation in both clusters. In the first cluster, the west coast ridge rapidly develops just prior to event onset along with the enhancement by southeastward directed WAF vectors off the west coast building internal energy (correspondingly, horizontal winds with the same orientation undergo strong sinking thereby building the warm anomaly in the TA area from compressional heating). The wave energy propagation across the North Pacific plays a crucial role in the formation of this first type of heat waves. Unlike the first cluster, height anomalies in the second cluster include a very strong pre-existing wave train across the north Pacific, including a ridge that covers most of NW America (height anomaly centered at the US-Canada coastal border) and lasts 3 days and more before the CCV heat wave onset. As time nears the onset of the CCV heat wave, the NW ridge center elongates eastward on its northern end and also southward to encompass the TA area. Interestingly, maximum anomaly of this ridge weakens while the North Pacific trough amplifies. The invigorated mid-ocean trough produces eastward WAF vectors on its southern side that enhance the southern expansion of the west coast ridge. Looking more broadly than the TA area, in the first cluster WAF is mainly directed east-southeastward in middle and high latitudes across the North Pacific with an equatorward component in the eastern Pacific. In the second cluster, by contrast, WAF is more zonal and directed eastward across the North Pacific over middle and subtropical latitudes for several days prior to onset including a significant subtropical Pacific trough near the Asian coast. The wavelengths in the wave train are longer in the second cluster. In short, the patterns at the onset, at least locally to the CCV, look similar in all events studied, but these results reveal two very different origins to those patterns.

Acknowledgements

This research was funded in part by NSF grant 1236681 and also supported by the USDA National Institute of Food and Agriculture, Hatch project CA-D-LAW-4264-H. . We also thank the anonymous peer reviewers for their helpful comments and feedback on the manuscript.

References

Alexander, L. V., P. Uotila, and N. Nicholls, 2009: Influence of sea surface temperature variability on global temperature and precipitation extremes. *Journal of Geophysical Research: Atmospheres (1984–2012)*, **114**.

Bachmann, B. A., 2008: The spatial extent of California heat waves. MS, University of California, Davis.

Bilby, T., L. Baumgard, R. Collier, R. Zimbelman, and M. Rhoads, 2008: Heat stress effects on fertility: Consequences and possible solutions. *Proc. Southwest Nutr. Conf*, 193-124.

Bumbaco, K. A., K. D. Dello, and N. A. Bond, 2013: History of Pacific Northwest Heat Waves: Synoptic Pattern and Trends*. *Journal of Applied Meteorology and Climatology*, **52,** 1618-1631.

Cellitti, M. P., J. E. Walsh, R. M. Rauber, and D. H. Portis, 2006: Extreme cold air outbreaks over the United States, the polar vortex, and the large-scale circulation. *Journal of Geophysical Research: Atmospheres (1984–2012)*, **111**.

Dee, D., and Coauthors, 2011: The ERA-Interim reanalysis: Configuration and performance of the data assimilation system. *Quarterly Journal of the Royal Meteorological Society*, **137,** 553-597.

Edmon, H., B. Hoskins, and M. McIntyre, 1980: Eliassen-Palm cross sections for the troposphere. *Journal of the Atmospheric Sciences*, **37,** 2600-2616.

Fischer, E. M., S. Seneviratne, P. Vidale, D. Lüthi, and C. Schär, 2007: Soil moisture-atmosphere interactions during the 2003 European summer heat wave. *Journal of Climate*, **20,** 5081-5099.

Gershunov, A., D. R. Cayan, and S. F. Iacobellis, 2009: The Great 2006 Heat Wave over California and Nevada: Signal of an Increasing Trend. *Journal of Climate*, **22,** 6181-6203.

Grossman-Clarke, S., J. A. Zehnder, T. Loridan, and C. S. B. Grimmond, 2010: Contribution of Land Use Changes to Near-Surface Air Temperatures during Recent Summer Extreme Heat Events in the Phoenix Metropolitan Area. *Journal of Applied Meteorology and Climatology*, **49,** 1649-1664.

Grotjahn, R., 2011: Identifying extreme hottest days from large scale upper air data: a pilot scheme to find California Central Valley summertime maximum surface temperatures. *Climate dynamics*, **37,** 587-604.

——, 2013: Ability of CCSM4 to simulate California extreme heat conditions from evaluating simulations of the associated large scale upper air pattern. *Climate dynamics*, **41,** 1187-1197.

Grotjahn, R., and M. Osman, 2007: Remote weather associated with North Pacific subtropical sea level high properties. *International journal of climatology*, **27,** 587-602.

Grotjahn, R., and G. Faure, 2008: Composite predictor maps of extraordinary weather events in the Sacramento, California, Region*. *Weather and Forecasting*, **23,** 313-335.

Grotjahn, R., and Coauthors, 2015: North American extreme temperature events and related large-scale meteorological patterns: A review of statistical methods, dynamics, modeling, and trends. *Climate Dynamics*.

Guirguis, K., A. Gershunov, R. Schwartz, and S. Bennett, 2011: Recent warm and cold daily winter temperature extremes in the Northern Hemisphere. *Geophysical Research Letters*, **38**.

Higgins, R. W., A. Leetmaa, and V. E. Kousky, 2002: Relationships between Climate Variability and Winter Temperature Extremes in the United States. *Journal of Climate*, **15,** 1555-1572.

Hirschi, M., and Coauthors, 2011: Observational evidence for soil-moisture impact on hot extremes in southeastern Europe. *Nature Geoscience*, **4,** 17-21.

Jeong, J.-H., C.-H. Ho, B.-M. Kim, and W.-T. Kwon, 2005: Influence of the Madden-Julian Oscillation on wintertime surface air temperature and cold surges in east Asia. *Journal of Geophysical Research: Atmospheres*, **110,** D11104.

Jones, T. S., and Coauthors, 1982: Morbidity and mortality associated with the July 1980 heat wave in St Louis and Kansas City, Mo. *Jama*, **247,** 3327-3331.

Kalnay, E., and Coauthors, 1996: The NCEP/NCAR 40-year reanalysis project. *Bulletin of the American Meteorological Society*, **77,** 437-471.

Lee, Y. Y., and R. X. Black, 2013: Boreal winter low-frequency variability in CMIP5 models. *Journal of Geophysical Research: Atmospheres*, **118,** 6891-6904.

Lim, Y. K., and S. D. Schubert, 2011: The impact of ENSO and the Arctic Oscillation on winter temperature extremes in the southeast United States. *Geophysical Research Letters*, **38**.

Loikith, P. C., and A. J. Broccoli, 2012: Characteristics of observed atmospheric circulation patterns associated with temperature extremes over North America. *Journal of Climate*, **25,** 7266-7281.

Loikith, P. C., and A. J. Broccoli, 2013: The Influence of Recurrent Modes of Climate Variability on the Occurrence of Winter and Summer Extreme Temperatures over North America. *Journal of Climate*, **27,** 1600-1618.

Meehl, G. A., C. Tebaldi, H. Teng, and T. C. Peterson, 2007: Current and future US weather extremes and El Niño. *Geophysical Research Letters*, **34**.

Nakamura, H., M. Nakamura, and J. L. Anderson, 1997: The Role of High- and Low-Frequency Dynamics in Blocking Formation. *Monthly Weather Review*, **125,** 2074-2093.

Park, T.-W., C.-H. Ho, and S. Yang, 2011: Relationship between the Arctic Oscillation and cold surges over East Asia. *Journal of Climate*, **24,** 68-83.

Plumb, R. A., 1986: Three-Dimensional Propagation of Transient Quasi-Geostrophic Eddies and Its Relationship with the Eddy Forcing of the Time—Mean Flow. *Journal of the Atmospheric Sciences*, **43,** 1657-1678.

Seber, G. A., 2009: *Multivariate observations.* Vol. 252, John Wiley & Sons.

Sillmann, J., M. Croci-Maspoli, M. Kallache, and R. W. Katz, 2011: Extreme cold winter temperatures in Europe under the influence of North Atlantic atmospheric blocking. *Journal of Climate*, **24,** 5899-5913.

Smith, A., and R. Katz, 2013: US billion-dollar weather and climate disasters: data sources, trends, accuracy and biases. *Nat Hazards*, **67,** 387-410.

Spath, H., 1985: *The cluster dissection and analysis theory fortran programs examples.* Prentice-Hall, Inc.

Stefanon, M., F. D'Andrea, and P. Drobinski, 2012: Heatwave classification over Europe and the Mediterranean region. *Environmental Research Letters*, **7,** 014023.

Takaya, K., and H. Nakamura, 2001: A formulation of a phase-independent wave-activity flux for stationary and migratory quasigeostrophic eddies on a zonally varying basic flow. *Journal of the Atmospheric Sciences*, **58,** 608-627.

Walsh, J. E., A. S. Phillips, D. H. Portis, and W. L. Chapman, 2001: Extreme cold outbreaks in the United States and Europe, 1948-99. *Journal of climate*, **14,** 2642-2658.

Wang, M., X. Yan, J. Liu, and X. Zhang, 2013: The contribution of urbanization to recent extreme heat events and a potential mitigation strategy in the Beijing–Tianjin–Hebei metropolitan area. *Theor Appl Climatol*, **114,** 407-416.

Westby, R. M., Y.-Y. Lee, and R. X. Black, 2013: Anomalous Temperature Regimes during the Cool Season: Long-Term Trends, Low-Frequency Mode Modulation, and Representation in CMIP5 Simulations. *Journal of Climate*, **26,** 9061-9076.

Wettstein, J. J., and L. O. Mearns, 2002: The Influence of the North Atlantic–Arctic Oscillation on Mean, Variance, and Extremes of Temperature in the Northeastern United States and Canada. *Journal of Climate*, **15,** 3586-3600.

Yin, D., M. L. Roderick, G. Leech, F. Sun, and Y. Huang, 2014: The contribution of reduction in evaporative cooling to higher surface air temperatures during drought. *Geophysical Research Letters*, **41,** 7891-7897.

Figures

Figure 1 Geographic location of 15 California Central Valley NCDC stations (marked by '+' symbols) used in our heat waves criteria

Figure 2 Scatter of two projection coefficients coefficients for each of the 28 events. The numbers match the event numbers specified in Table 1. A dot marks each event in cluster one, a circled number for each event in cluster two, and mixed events are marked with a '+' symbol. For individual events, three anomalous fields (-2day zonal wind at 700 hPa, -2day temperature at 600 hPa, and -1day temperature at 700 hPa) are projected onto their composites of two clusters over 150W-100W, 20N-60N domain, then the average of three coefficients are plotted. Five undetermined and/or mixed events are excluded from the analysis afterward.

Figure 3 anomalous composite of (contour) air temperature, (vector) horizontal wind, and (shading) omega (or pressure velocity) for cluster one. For all three fields, only grid points which have sign counts with magnitude over 1/3 of cluster member numbers are plotted. Vectors are plotted at the grids where either zonal or meridional component is passing 1/3 sign counts criteria. Contour interval is 0.7 K (3.5 K for thick contours). The unit of shading is Pascal/s. For the clarity, only positive omega shadings come with contours.

Figure 4 Same as in Figure 3 but for cluster two.

Figure 5 Composite of (contour) air temperature anomalies, (vector) total horizontal wind, and (shading) total omega for cluster one. For the air temperature anomalies, only grid points which have sign counts with magnitude over 1/3 of cluster member numbers are plotted. Contour interval is 0.7K (3.5 K for thick contours). The unit of shading is Pascal/s. For the clarity, only positive omega shadings come with contours.

Figure 6 same as in Figure 5 but for cluster two.

Figure 7 Backwards trajectories of the 28 events: 2-D projections onto longitude-latitude, latitude-pressure, and longitude-pressure domain over 4 days prior to onset. The numbers refer to the event numbers specified in Table 1. Cluster one events trajectories use a dark grey dotted line. Cluster two events use a black solid line. Trajectories for mixed events that are not strongly matched with either cluster are drawn with a light grey solid line.

Figure 8 Box and whisker plots comparing area average values in selected regions, levels, and times for the indicated anomaly fields shown in Figs. 3 and 4. In each panel the left pair is for cluster one and the right pair is for cluster two. In each pair the left member is calculated from the ERA-interim reanalyses while the right member is calculated from NNRA1 data. Each box brackets the middle 50% while the horizontal line within the box is the median value. Whiskers connect the highest and lowest values. Panel labels indicate level, time before onset, north latitude range, and east longitude range. Panels a) – c) are at earlier times and regions in proximity to the TA region showing consistency among cluster members but different cluster distributions.

Figure 9 composite of (contour) geopotential height anomaly and (vector) total horizontal wave activity flux for two clusters at 500 hPa. Shading indicates significant area of geopotential height by plotting the grid points which have sign counts whose magnitude exceeds 1/3. Wave activity flux are plotted only when at least one of zonal and meridional component has sign counts whose magnitude exceeds 1/3. Contour interval is 20m.

Figure 10 Composite of (thick contour) total zonal winds and (thin contour) anomalous zonal winds at 250 hPa. For the anomaly field, grid points are plotted only when the sign count has magnitude greater than 1/3 of cluster member numbers. Contour interval is 2 ms-1 for anomaly field and 6 ms-1 for total field. The minimum contour of total field is 18 ms-1.

Tables

Table 1 Start/end dates and duration of 28 CCV hot spells considered

Table 1 Start/end dates and duration of 28 CCV hot spells considered

Event #	Event Start date	Event End date	Duration (days)
*1	"06-05-1977"	"06-07-1977"	3
*2	"09-06-1977"	"09-08-1977"	3
†3	"06-05-1978"	"06-07-1978"	3
4	"08-05-1978"	"08-09-1978"	5
*5	"09-12-1979"	"09-17-1979"	6
6	"07-24-1980"	"07-27-1980"	4
*7	"06-11-1985"	"06-17-1985"	7
*8	"07-17-1988"	"07-19-1988"	3
†9	"08-25-1988"	"08-27-1988"	3
†10	"09-03-1988"	"09-06-1988"	4
†11	"07-12-1990"	"07-14-1990"	3
12	"08-05-1990"	"08-10-1990"	6
*13	"07-02-1991"	"07-05-1991"	4
†14	"06-02-1992"	"06-04-1992"	3
†15	"08-16-1992"	"08-20-1992"	5
*16	"06-02-1996"	"06-07-1996"	6
†17	"08-10-1996"	"08-15-1996"	6
*18	"08-03-1998"	"08-05-1998"	3
†19	"08-30-1998"	"09-03-1998"	5
†20	"09-18-2000"	"09-20-2000"	3
*21	"07-10-2002"	"07-12-2002"	3
*22	"06-22-2006"	"06-24-2006"	3
*23	"07-20-2006"	"07-26-2006"	7
*24	"07-07-2008"	"07-10-2008"	4
*25	"08-27-2008"	"08-29-2008"	3
26	"09-05-2008"	"09-07-2008"	3
†27	"09-25-2009"	"09-27-2009"	3
28	"09-27-2010"	"09-29-2010"	3
*1st cluster avg.			4.2
†2nd cluster avg.			3.8
*1st cluster std.			1.6
†2nd cluster std.			1.1

*(†) Events which are assigned in Cluster #1(#2). Event without a superscript are 'mixed' type and could not be assigned strongly to either cluster.

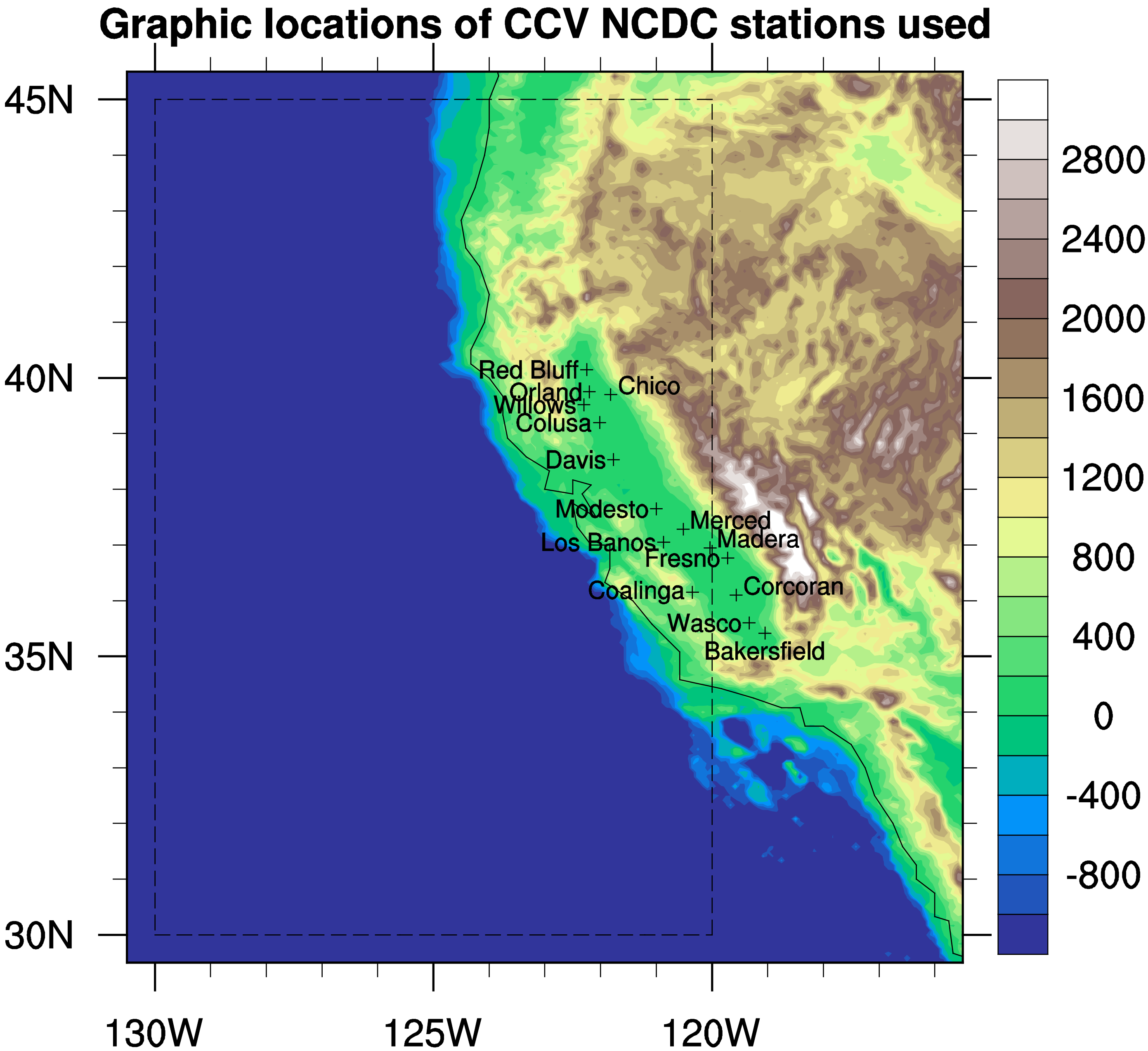

Figure 1 Geographic location of 15 California Central Valley NCDC stations (marked by '+' symbols) used in our heat waves criteria. The boxed region with long-dash represents "TA area"..

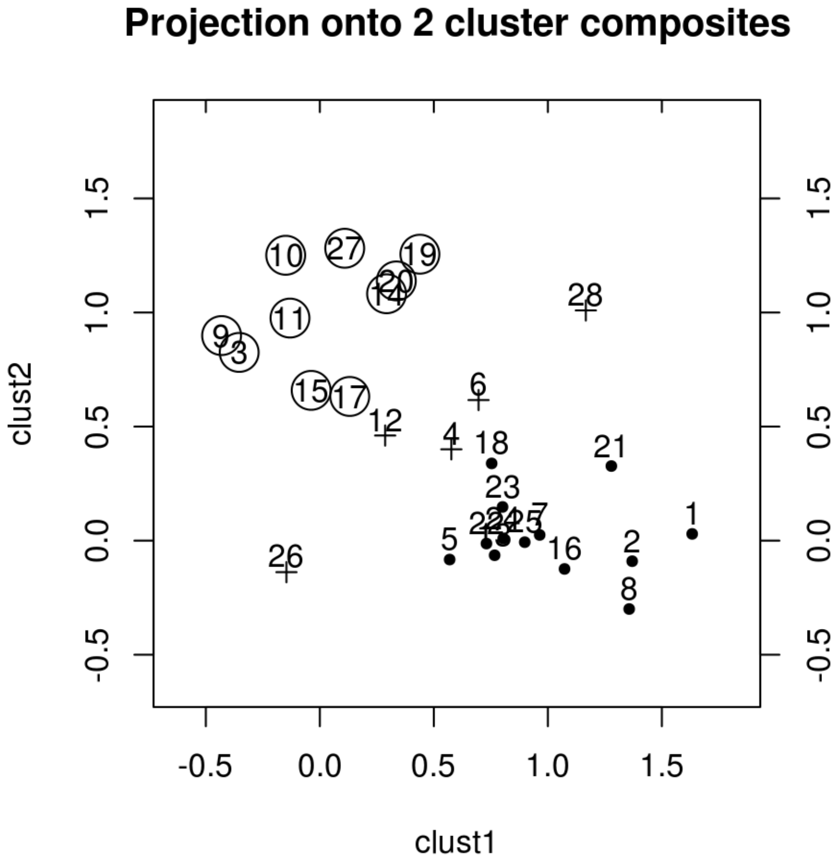

Figure 2 Scatter of two projection coefficients coefficients for each of the 28 events. The numbers match the event numbers specified in Table 1. A dot marks each event in cluster one, a circled number for each event in cluster two, and mixed events are marked with a '+' symbol. For individual events, three anomalous fields (-2day zonal wind at 700 hPa, -2day temperature at 600 hPa, and -1day temperature at 700 hPa) are projected onto their composites of two clusters over 150W-100W, 20N-60N domain, then the average of three coefficients are plotted. Five undetermined and/or mixed events are excluded from the analysis afterward.

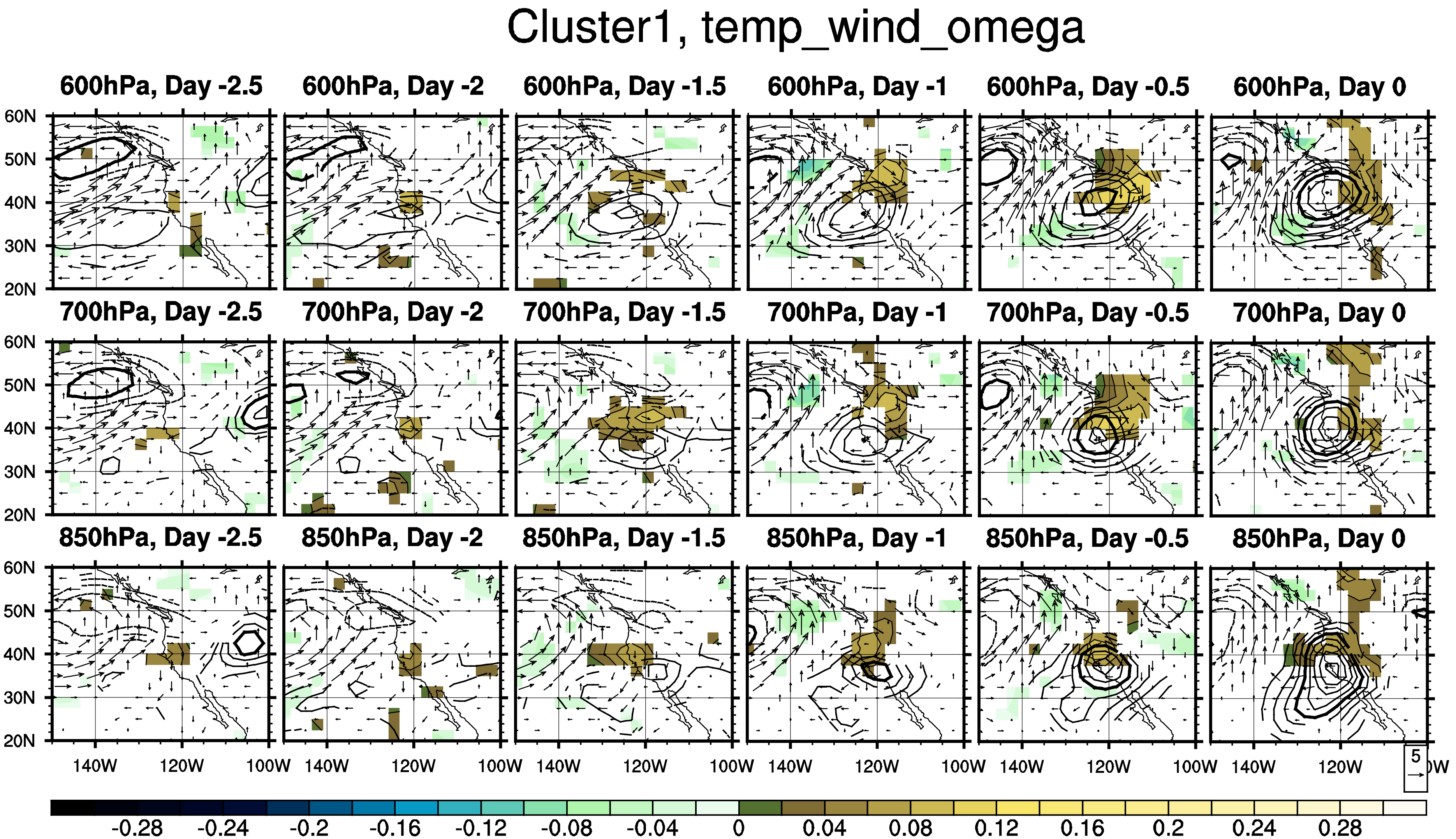

Figure 3 anomalous composite of (contour) air temperature, (vector) horizontal wind, and (shading) omega (or pressure velocity) for cluster one. For all three fields, only grid points which have sign counts with magnitude over 1/3 of cluster member numbers are plotted. Vectors are plotted at the grids where either zonal or meridional component is passing 1/3 sign counts criteria. Contour interval is 0.7 K (3.5 K for thick contours). The unit of shading is Pascal/s. For the clarity, only positive omega shadings come with contours.

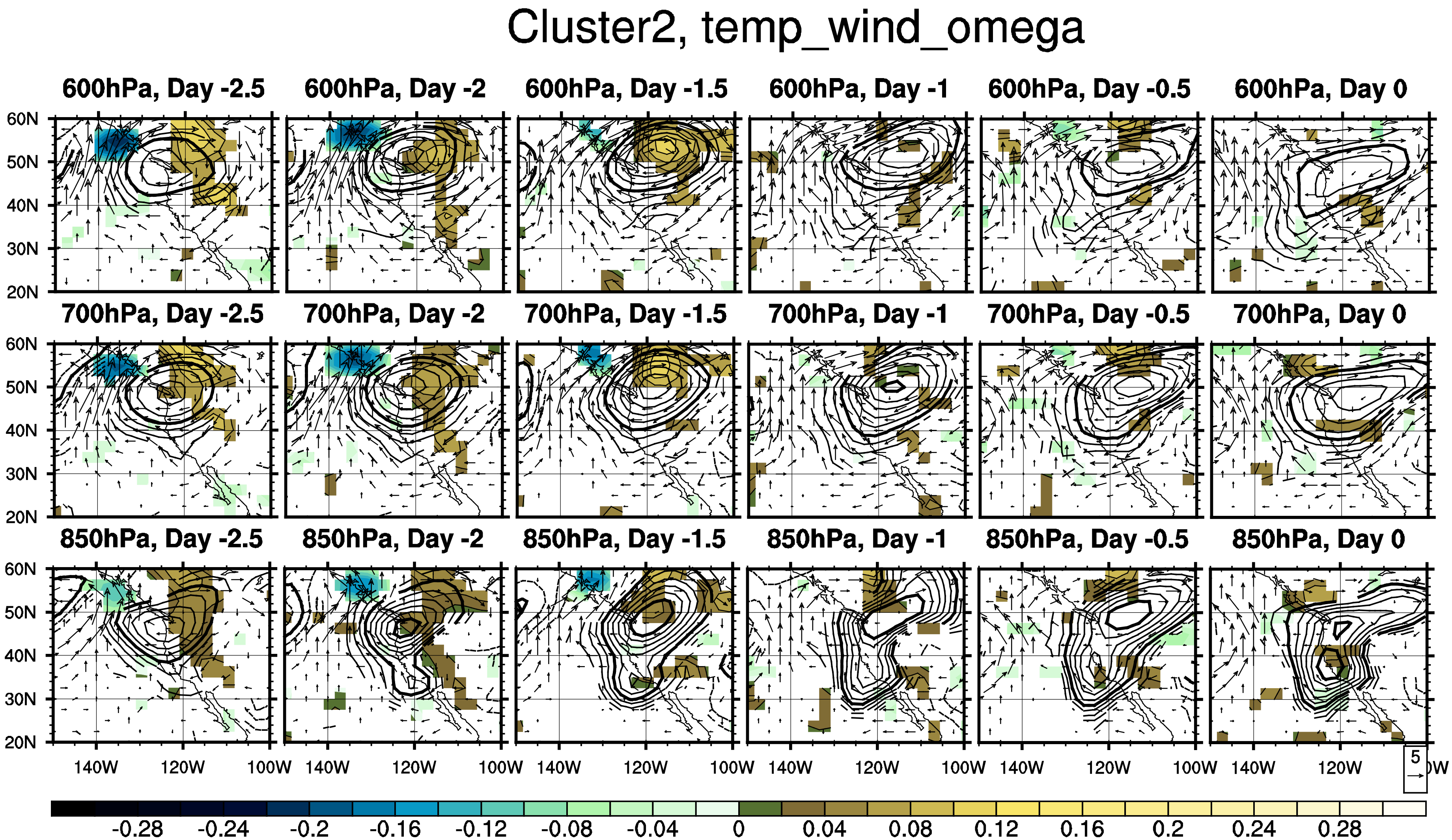

Figure 4 Same as in Figure 3 but for cluster two.

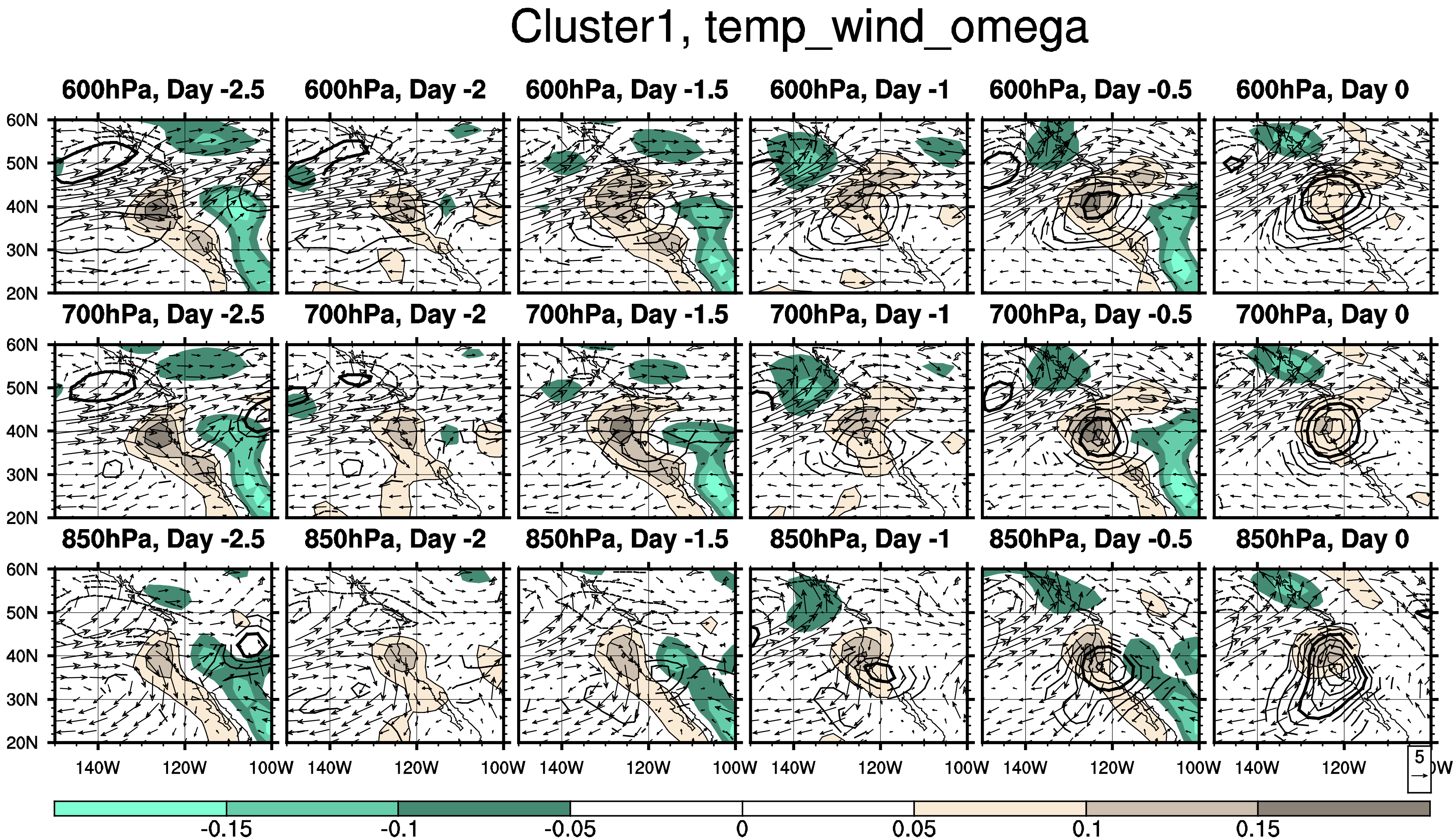

Figure 5 Composite of (contour) air temperature anomalies, (vector) total horizontal wind, and (shading) total omega for cluster one. For the air temperature anomalies, only grid points which have sign counts with magnitude over 1/3 of cluster member numbers are plotted. Contour interval is 0.7K (3.5 K for thick contours). The unit of shading is Pascal/s. For the clarity, only positive omega shadings come with contours.

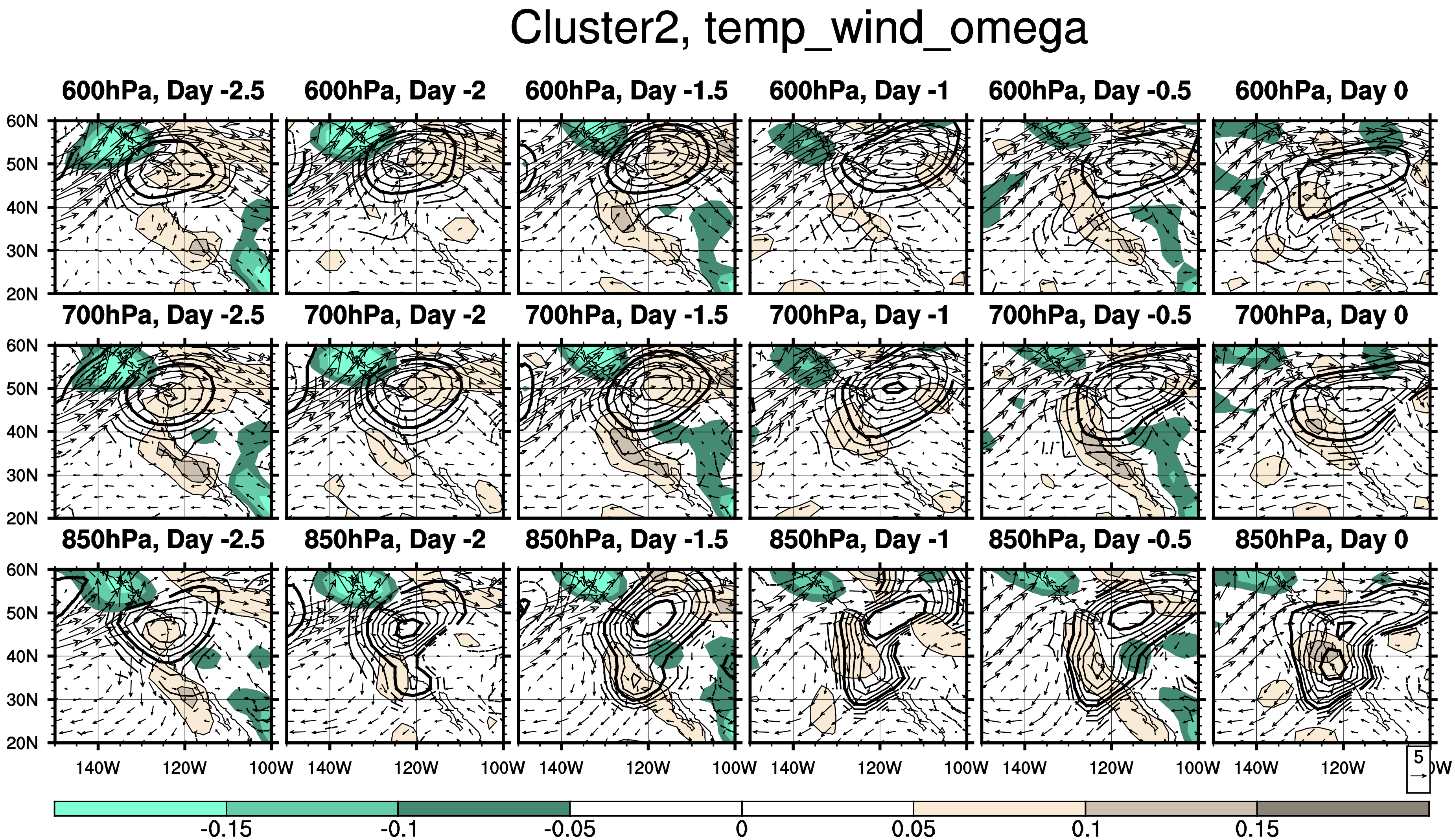

Figure 6 same as in Figure 5 but for cluster two.

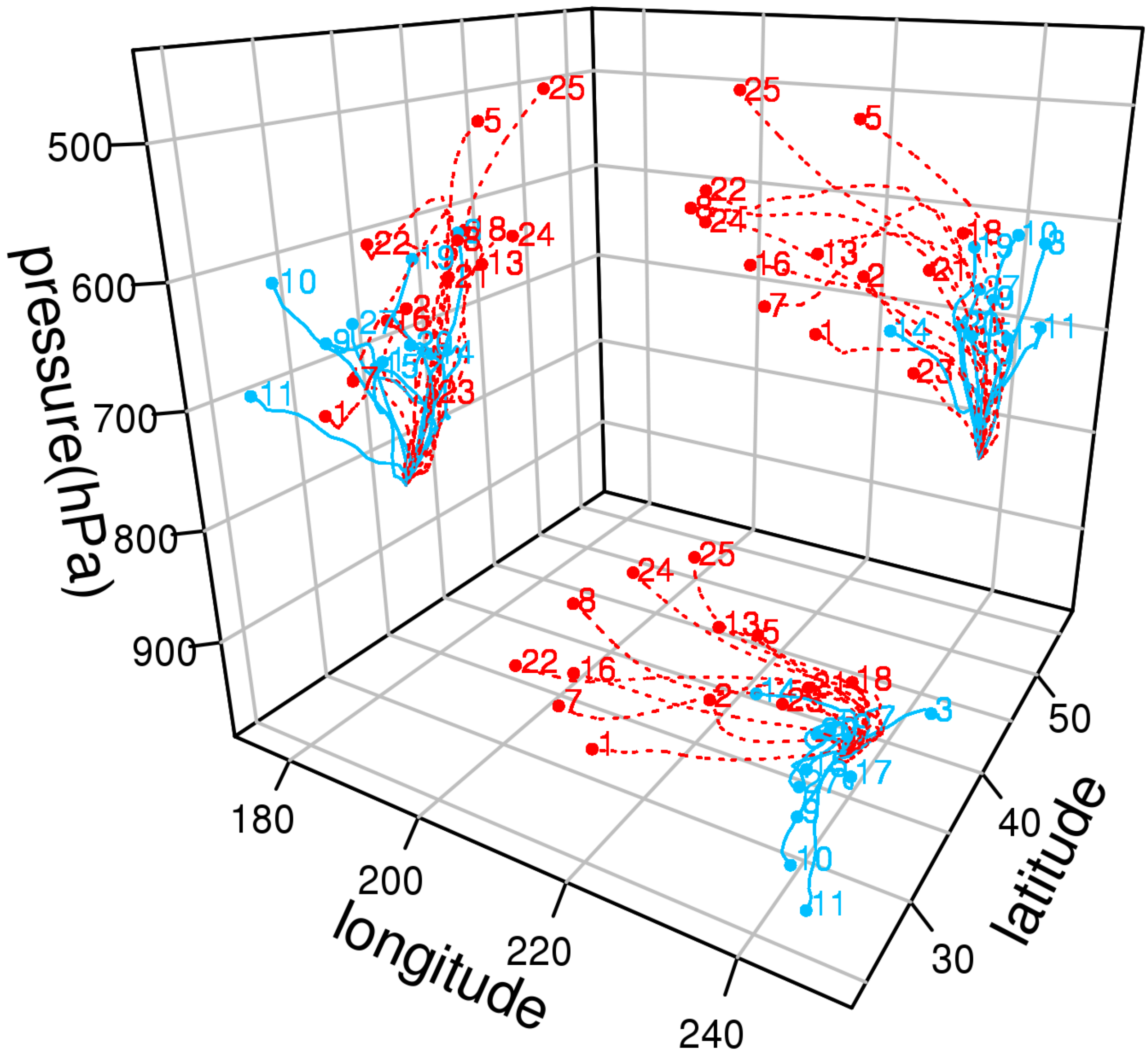

Figure 7 Backwards trajectories of the 28 events: 2-D projections onto longitude-latitude, latitude-pressure, and longitude-pressure domain over 4 days prior to onset. The numbers refer to the event numbers specified in Table 1. Cluster one events trajectories use a dark grey dotted line. Cluster two events use a black solid line. Trajectories for mixed events are not drawn here.

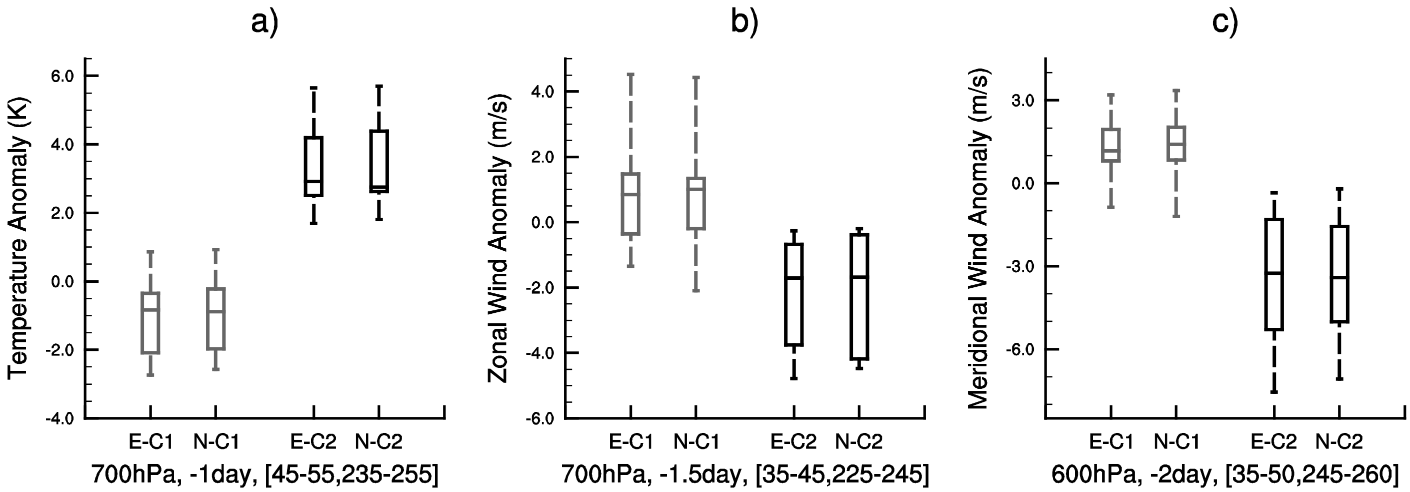

Figure 8 Box and whisker plots comparing area average values in selected regions, levels, and times for the indicated anomaly fields shown in Figs. 3 and 4. In each panel the left pair is for cluster one and the right pair is for cluster two. In each pair the left member is calculated from the ERA-interim reanalyses while the right member is calculated from NNRA1 data. Each box brackets the middle 50% while the horizontal line within the box is the median value. Whiskers connect the highest and lowest values. Panel labels indicate level, time before onset, north latitude range, and east longitude range. Panels a) – c) are at earlier times and regions in proximity to the TA region showing consistency among cluster members but different cluster distributions.

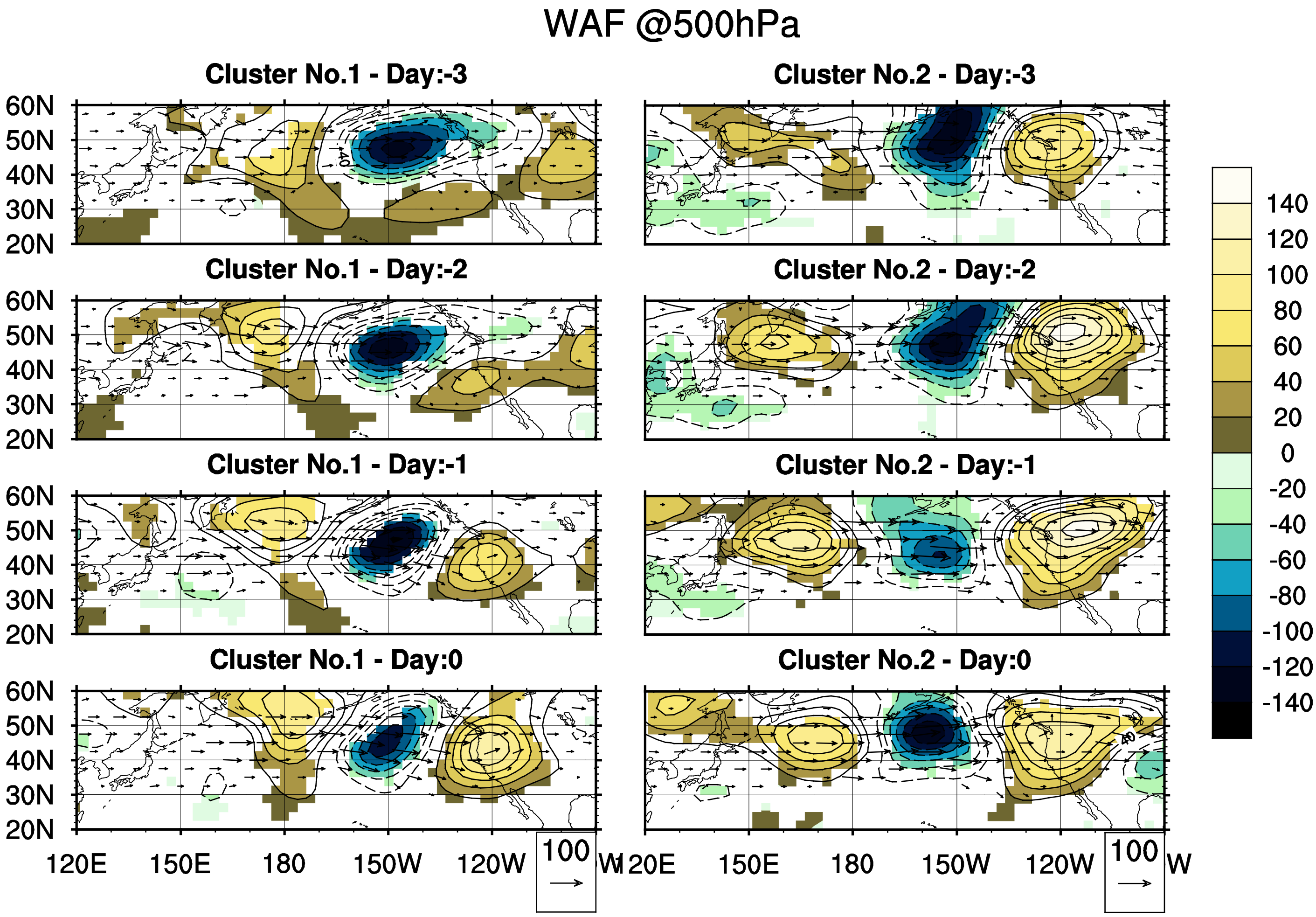

Figure 9 composite of (contour) geopotential height anomaly and (vector) total horizontal wave activity flux for two clusters at 500 hPa. Shading indicates significant area of geopotential height by plotting the grid points which have sign counts whose magnitude exceeds 1/3. Wave activity flux are plotted only when at least one of zonal and meridional component has sign counts whose magnitude exceeds 1/3. Contour interval is 20m.

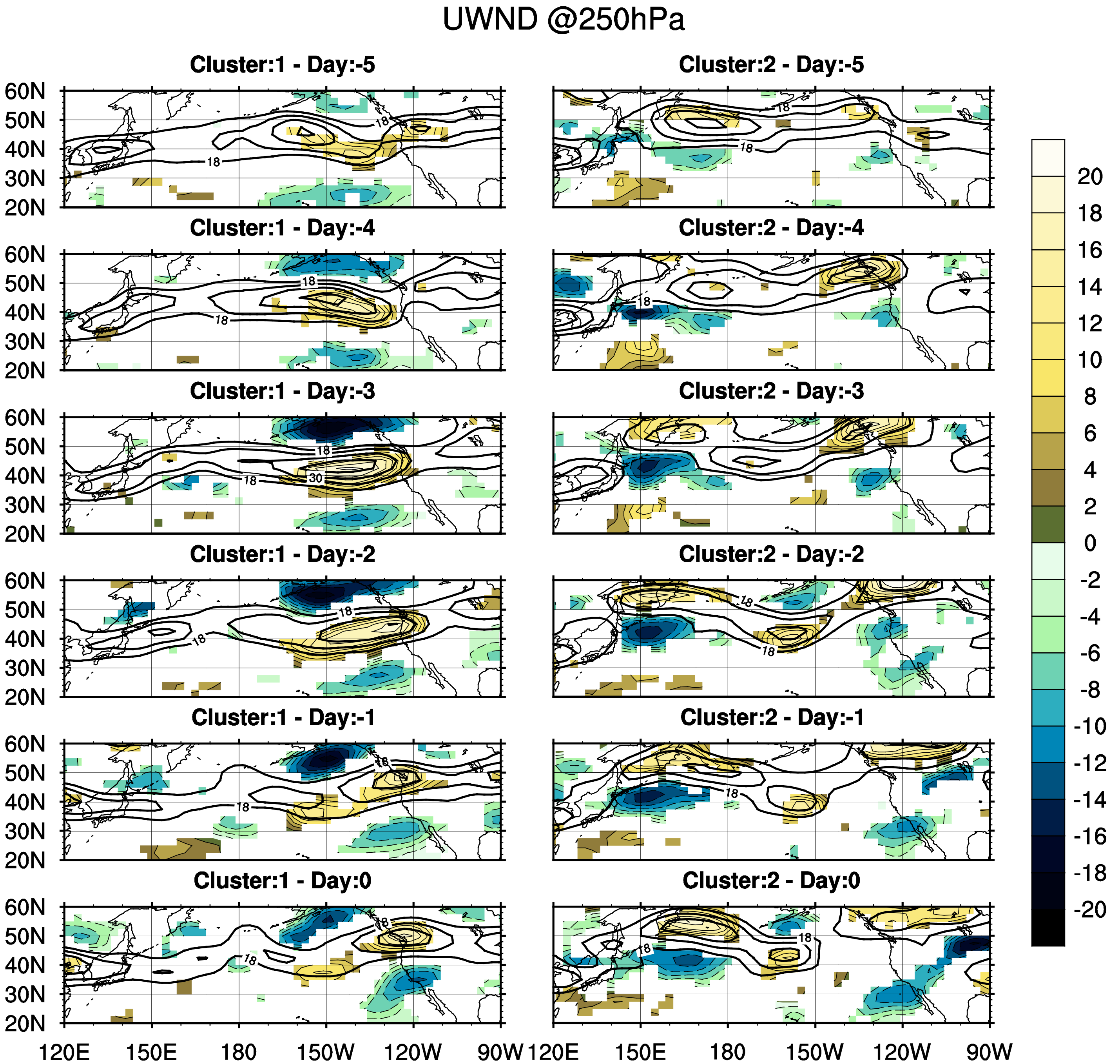

Figure 10 Composite of (thick contour) total zonal winds and (thin contour) anomalous zonal winds at 250 hPa. For the anomaly field, grid points are plotted only when the sign count has magnitude greater than 1/3 of cluster member numbers. Contour interval is 2 ms^{-1} for anomaly field and 6 ms^{-1} for total field. The minimum contour of total field is 18 ms^{-1}.